Acta Biomaterialia 108 (2020) 313–325

Contents lists available at ScienceDirect

Acta Biomaterialia

journal homepage: www.elsevier.com/locate/actbio

Full length article

Biogenic nanobubbles for effective oxygen delivery and enhanced photodynamic therapy of cancer

Lin Song, Guohao Wang, Xuandi Hou, Shashwati Kala, Zhihai Qiu, Kin Fung Wong, Fei Cao, Lei Sun*

Department of Biomedical Engineering, The Hong Kong Polytechnic University, Hung Hom, Hong Kong Special Administrative Region

ARTICLE INFO

Article history:
Received 19 November 2019
Revised 21 March 2020
Accepted 24 March 2020
Available online 5 April 2020

Keywords:
Oxygen delivery
Nanobubbles
Gas vesicles
Tumor hypoxia
Photodynamic therapy

ABSTRACT

Tumor hypoxia is believed to be a factor limiting successful outcomes of oxygen-consuming cancer therapy, thereby reducing patient survival. A key strategy to overcome tumor hypoxia is to increase the prevalence of oxygen at the tumor site. Oxygen-containing microbubbles/nanobubbles have been developed to supply oxygen and enhance the effects of therapies such as radiotherapy and photodynamic therapy. However, the application of these bubbles is constrained by their poor stability, requiring major workarounds to increase their half-lives. In this study, we explore the potential of biogenic gas vesicles (GVs) as a new kind of oxygen carrier to alleviate tumor hypoxia. GVs, which are naturally formed, gas-filled, protein-shelled compartments, were modified on the surface of their protein shells by a layer of liposome. A substantial improvement of oxygen concentration was observed in hypoxic solution, in hypoxic cells, as well as in subcutaneous tumors when lipid-GVs(O_2) were added/tail-injected. Significant enhancement of tumor cell apoptosis and necrosis was also observed during photodynamic therapy (PDT) in the presence of lipid-GVs(O_2) both *in vitro* and *in vivo*. Lipid-GVs(O_2) alone induced no obvious change in cell viability *in vitro* or any apparent pathological abnormalities after mice were tail-injected with them. In all, lipid-GVs exhibited promising performance for intravenous gas delivery, enhanced PDT efficacy and low toxicity, a quality that may be applied to alleviate hypoxia in cancers, as well as hypoxia-related clinical treatments.

Statement of significance

The development of stable oxygen-filled micro/nanobubbles capable of delivering oxygen to tumor sites is a major hurdle to enhancing the efficacy of cancer therapy. Currently, micro/nanobubbles are limited by their instability when oxygen is encapsulated, creating a large pressure gradient and surface tension. To improve stability, we modified the surfaces of GVs, a biogenic stable nanoscale hollow structure, as a new class of oxygen carriers. Lipid-coated GVs were found to be stable in solution and effective O_2 carriers. This will overcome the limitations of coalescence, short circulation time of synthetic bubbles during application. Our surface-modified GVs demonstrated low toxicity *in vitro* cell *in vivo*, while also being able to overcome hypoxia-associated therapy resistance when combined with photodynamic therapy.

1. Introduction

The existence of hypoxia is a common characteristic of most solid tumors, caused by low vascular density, irregular vascular geometry and an imbalance between oxygen consumption and supply at the tumor site. This often compromises any cancer therapies that may be applied. Hypoxic cells are more resistant to radiotherapy, chemotherapy and other oxygen-consuming therapies such as photodynamic therapy (PDT) [1,2]. This is exacerbated by the fact that hypoxia is closely associated with a high risk of metastasis, further worsening therapeutic outcomes. Given hypoxia's obstructive role, tumor oxygenation is considered an important auxiliary

---

* Corresponding author.
E-mail addresses: lei.sun@polyu.edu.hk, lin.song@connect.polyu.hk (L. Sun).

https://doi.org/10.1016/j.actbio.2020.03.034

method for anticancer therapy [3,4]. Tumor oxygenation has been tried in two primary ways: increasing blood oxygenation in general or increasing oxygen delivery at the tumor site. Hyperbaric oxygen (HBO) and hyperbaric carbogen are common ways to reduce tumor hypoxia by increasing the amount of dissolved oxygen in blood throughout the body [5–7]. However, not only are these methods prohibitively expensive, their generic, untargeted nature could lead to severe deleterious off-target side-effects. An alternative approach is to use molecular oxygen carriers, that can bind oxygen with high affinity and enable rapid and targeted tissue delivery. Perfluorocarbon (PFC) emulsions and acellular hemoglobin-based oxygen carriers (HBOCs) were initial attempts at oxygen delivery to tumors. Unfortunately, such carriers failed due to their merely marginal benefits and severe side effects in clinical trial [8–10].

More recently, efforts have been made to develop synthetic microparticles and nanoparticles such as oxygen-filled microbubbles and nanoparticle-based HBOCs. Notably, oxygen-filled lipid microbubbles have shown good capability as oxygen carriers [11–13]. These microbubbles, usually coated with a layer of lipid, can hold large amounts of oxygen in their gas core. Microbubbles have also been demonstrated to change the hypoxic microenvironment *in vivo* and enhance outcomes for chemotherapy and radiotherapy [12,14–17]. Thus, oxygen-filled microbubbles constitute a promising new way to deliver oxygen to hypoxic tumor sites for therapeutic purposes. However, despite their effectiveness in delivering oxygen to tissues, various studies also revealed critical limitations in their anticancer abilities. Microbubbles have limited intravascular dwell time due to their relatively large sizes ($>$ 1 µm). Thus, repetitive administration is required for continuous oxygen delivery, which increases the viscosity of serum and causes long-term toxicity in blood and tissues [18,19]. Lipid microbubbles may also suffer from stability issues such as dissolution and coalescence when entering the circulation, correlated with greater product loss, possibly leading to excessive production of reactive oxygen species (ROS) and adverse oxidative stress [15,20,21]. Such lipid microbubbles are, thus, not ideal candidates for oxygenation of tumor tissues in the body. Stable oxygen-filled nanobubbles which do not undergo dissolution and coalescence may provide an alternative that could overcome the aforementioned limitations of microbubbles. Nanobubbles are established as having long intravascular dwell times, and their smaller size could exploit enhanced permeability and retention (EPR) effects to pass through the leaky vasculature of tumors to deeper sites [15,22]. These properties enable nanobubbles to stay longer and go deeper into the tumor site, paving the way for potential improvement of clinical outcome [23,24]. Nanobubbles such as dextran nanobubbles, polymer, and lipid nanobubbles have also been developed for oxygen delivery in initial studies [25–29]. Nevertheless, limitations such as instability and relatively lower half-life also exist for those synthetic nanobubbles.

Gas vesicles (GVs), a nanoscale hollow structure, have recently been reported as the first biomolecular acoustic reporters with gene editability and inherent stability [30–34]. In contrast to synthetic nanobubbles, GVs naturally occur gas-filled cavities formed by cyanobacteria or archaea as a means to control buoyancy for optimal access to light and nutrients in the water. They are hollow protein shells with sizes different from 200 to 400 nm [35]. The mechanism to load GVs with gases is significantly different from that of regular microbubbles/nanobubbles. Typically, microbubbles/nanobubbles depend on the lipid shell to encapsulate gases, creating a gradient between internal and external pressure, and the addition of surfactant stabilizers is needed to stabilize them [18,19]. However, the walls of GVs exclude water but allow gas to permeate in and out the shells freely. Hence, only a minimal pressure gradient is created, allowing GVs significantly greater stability than nanoscale bubbles [30,35]. Additionally, the protein surface of GVs is amenable to modification, and this could be used to endow GVs with additional physical or chemical properties that may help them to be better oxygen carriers [36].

To attain better oxygen delivery efficacy, we fabricated lipid coated GVs and investigated their ability as a new platform to elevate oxygen concentration in hypoxic tumor sites. We found the GVs to be nanosized and stable in solution over 6 months. We evaluated whether lipid-GVs(O_2) administration treatment could alleviate hypoxia both in cultured cells and in a hypoxic tumor model and found that they significantly improved oxygen delivery compared to native GVs(O_2). Furthermore, we verified the effects of lipid-GVs(O_2) using photodynamic therapy (PDT). PDT is an oxygen-consuming therapy and the efficacy of PDT is dependent on oxygen related generation of ROS [37–42]. The presence of lipid-GVs(O_2) significantly improved ROS production and reduced cell viability in combination with PDT compared to PDT alone, while causing no notable toxicity by themselves. This combination PDT treatment also significantly reduced tumor size *in vivo* and increased the number of apoptotic cells, with obvious damage visible in excised tumors. Thus, this study lays the groundwork for lipid-coated GVs as an oxygen-delivery vehicle to safely enhance the efficacy of PDT.

2. Materials and methods

2.1. Preparation, surface modification and characterization of lipid-GVs

Anabaena flos-aquae (FACHB-I255, Freshwater Algae Culture Collection at the Institute of Hydrobiology, China) were cultured in sterile BG-11 Medium (Sigma, St. Louis, MO, USA) at 25 °C under fluorescent lighting with I4hr/10hr light/dark duty cycle. Algae were hypertonic lysed with a 25% concentration of sucrose solution when they became mature, and GVs were then released from the algae. GVs were then isolated by centrifugation at 600 g for 3 h and isolated GVs could form a white layer on the top of the solution after centrifugation. GVs was purified three times with phosphate-buffered saline (PBS) and stored in PBS at 4 °C. The concentration of GVs was measured by optical density method characterized by 500 nm wavelength light (OD500) by UV–Visible spectrophotometer (2100 pro, GE Healthcare Ltd, Piscataway, NJ, USA) and calculated to mole concentration with the ratio of 450 pM/OD500 [30].

To modify the GVs surfaces, 6 µl of 18 mg/ml dioleoyl phosphatidylcholine (DOPC) (Thermo Fisher Scientific, MA, USA) was dissolved in 2 ml chloroform (Thermo Fisher Scientific, MA, USA) in a 25 ml round-bottom flask. The solvent was then evaporated and the samples were dried in a vacuum rotary evaporator. 1 ml of 20 mM HEPES buffer (pH = 7.2, Thermo Fisher Scientific, MA, USA) was then added to the dried lipid layer, forming a cloudy solution after vigorous agitation. The mixture was then probe-sonicated (20 W, 15 s pulses for 20 min) for 3–5 min until the solution became clear. The resulting liposome solution was stored at 4 °C for further use. 1 ml prepared liposome solution was added to 1 ml of 1 nM GV solution and incubated overnight on a rocker platform. GVs were then washed three times by centrifugation (24,000 rpm, 10 min) and resuspended in PBS. Finally, lipid-GVs were resuspended in PBS for use in experiments [43–45].

In order to understand the biodistribution of lipid-GVs *in vivo*, indocyanine green (ICG) (Sigma-Aldrich, St.Louis, MO) was used to label lipid-GVs. ICG was added during liposome preparation at a ratio of 20 µg ICG:5 nM lipid-GVs. To completely incorporate ICG into the lipid membrane, ICG dissolved in 100% CH_3OH was added to the lipid mixture prior to it being dried into a thin film [46].

Light exposure was avoided during fabrication of ICG labeled lipid-GVs.

For characterization of GVs, size distribution and zeta potentials were determined by laser light scattering using a 90 Plus instrument (Brookhaven, Holtsville, NY, USA) at a fixed angle of 90° and a temperature of 25 °C. UV–Vis absorbance spectra of ICG and ICG-lipid-GVs were determined by a Multiskan Go microplate reader (Thermo Fisher Scientific, Massachusetts, USA). The size and morphology were determined by Transmission Electron Microscopy (TEM) with the operating voltage of 200 kV. Samples of GVs (OD 0.1) were deposited on a carbon-coated formvar grid. To measure the stability of GVs, single particle size and concentration of the formulation were determined in the first month and the sixth month, respectively.

2.2. Determination of oxygen release kinetics of lipid-GVs in solution

The oxygen concentration in the solution was monitored using an oxymeter (Portamess 913 OXY, Knick, Germany) and the data were recorded as mg/l. Before each experiment, the oxymeter was calibrated in air, after waiting for stable temperature and humidity conditions to be re-established. Oxygen filled PBS (PBS(O_2)), oxygen filled GVs (GVs(O_2)), and oxygen filled lipid-GVs(lipid-GVs(O_2)) were prepared by a continuous oxygen purge for 20 min. To determine oxygen release kinetics of GVs, 1 ml PBS(O_2), GVs(O_2) or lipid-GVs(O_2) (filled with oxygen, sealed into vials) were injected into the 5 ml hypoxic solution and the oxygen concentration of the solution was monitored over time. The hypoxic solution was obtained by a continuous N_2 purge until the oxygen concentration in PBS was finally reduced to 0.8 mg/l (severe hypoxia). All the experiments were performed in triplicate.

2.3. In vitro *O_2 delivery test of lipid-GVs(O_2)*

Human hepatoma cell line (HepG2) were obtained from the cell bank of the Chinese Academy of Science, Shanghai, China. HepG2 were cultured in high-glucose (4.5 g/l) Dulbecco's modified Eagle's medium with L-glutamine (Thermo Fisher Scientific, MA, USA) following standard cell culture instructions. All media were supplemented with 10% (vol/vol) fetal bovine serum, penicillin (100 U/mL) and streptomycin (100 µg/ml) (Thermo Fisher Scientific, MA, USA). Cells were grown at 37 °C in a 5% CO_2 and 95% air atmosphere until 70%−80% confluence before trypsinization and harvesting for *in vitro* studies. For hypoxia detection, cells were cultured in a hypoxic chamber (1% oxygen, 5% CO_2) overnight before the experiment. Hypoxic conditions in the media were monitored using Image-iT^{TM} Red Hypoxia Reagent (5 µM) bought from Thermo Fisher. This hypoxia reagent could measure hypoxia in live cells and it is non-fluorescent when live cells are in an environment with normal oxygen concentration and show fluorescent when oxygen levels decrease. Besides, it is a real-time oxygen detector with a fluorogenic response changes according to the surrounding oxygen levels. The reagent was added into the medium and co-cultured with cells at the beginning of the experiment and the fluorescence of the reagent was monitored before/after the addition of lipid-GVs(O_2). lipid-GVs(O_2) (1 nM) were co-cultured with cells for an hour during the experiments. Cells were then visualized under laser-scanning confocal microscopy with X63 objective (Nikon, Tokyo, Japan) and the intensity of fluorescence was quantified by Image J.

2.4. In vitro *photodynamic therapy*

5-aminolevulinic acid (ALA) which was obtained from Sigma (St Louis, MO, USA) was used in this experiment as the photosensitizer. It was dissolved in PBS to a stock concentration of 1 M and was stored in the dark at −20 °C. For the ALA treatment, cells were incubated with 1 mM ALA for a 4 h drug-loading time in DMEM medium supplemented with 10% FBS. The optical setup for PDT treatment is shown in Fig. 5A. Cells under PDT treatment were exposed to laser with a power of 100 mW/cm^2 for 5 min. The light source was generated with a wavelength of 405 nm by an optical fiber was collimated to an aperture and irradiated to the 35 mm cell culture dish. The position of the cell culture plate was manually controlled by a two-axis motorized linear stage. After the treatment, the cells were cultured in fresh medium for different times and then prepared for different analyses.

2.5. Cell viability, apoptosis, and intracellular ROS production assay

Cell viability at 4 h following PDT was determined using a Cell Counting Kit-8 (Sigma-Aldrich) according to the manufacturer's instructions. Briefly, cells were plated at a density of 5000 cells per well in a 96-well plate and incubated in 100µl culture medium for 24 h. Cytotoxicity was determined by adding 10µl CCK-8 reagent per well for 1 h at 37 °C in 5% CO_2. The absorbance of the treated samples against a blank control was measured at 450 nm as the detection wavelength. The viability of treated cells was determined by comparing to the untreated ones in the control group. Alexa Fluor 488 Annexin V/Dead Cell Apoptosis Kit (Thermo Fisher Scientific) was used to measure cell apoptosis 4 h following PDT according to the manufacturer's instructions. Cells were seeded at a density of 5×10^5 cells in 6-cm dishes and incubated for 24 h. Cells were collected and incubated with 5µl of the annexin V conjugate and 1µl of the PI working solution at room temperature for 15 min. Intracellular ROS production was measured 1 h following PDT treatment using DCFH-DA (Sigma-Aldrich). Briefly, 10 µM DCFH-DA diluted with PBS were added to cells at 37 °C for 20 min. Cells were then washed with PBS three times. Labeled cells were trypsinized and analyzed by flow cytometry. The cells were analyzed on the BD FACS Calibur flow cytometer and BD Accuri C6 Software (Becton-Dickinson, USA).

2.6. Assay of lipid-GVs' biodistribution in vivo

All procedures using laboratory animals were approved by the Department of Health, The Government of the Hong Kong Special Administrative Region and the Hong Kong Polytechnic University Animal Subjects Ethics Sub-committee. Female athymic nude mice weighing 16–18 g were supplied by the Animal Resource Centre of The University of Hong Kong. The mice were acclimated to the room for one week after arrival and were maintained on a normal 12 h light-dark cycle. The mice were housed in conventional cages (6 animal/cage) with free access to standard pellet diet and water in specific pathogen-free condition with 24±2 °C temperature, 60–70% relative humidity. Standard wood chips for mice were used as bedding material. After 1 week's acclamation, 4×10^6 squamous cell carcinoma cell line (SCC7) in PBS (80 µl) was injected into the rear dorsal of nude mice by subcutaneous injection. Tumor formation occurred approximately two weeks after cell implantation and we began imaging and therapy when tumor volume reached around 300 mm^3.

Mice were randomized into three groups: (a) PBS, (b) Free ICG solution, (c) ICG-labeled lipid-GVs. The respective solutions were injected into the tail veins of mice. Fluorescence images were acquired at 0, 5 min, 30 min, 1 h, 2 h after injection using IVIS Lumina II (Caliper Life Sciences, USA; Excitation Filter: 780 nm, Emission Filter: 800 nm). Tumors and normal organs (heart, liver, spleen, lung, and kidney) were collected at different timepoints after injection, and the fluorescent signal intensities of these organs were determined.

2.7. In vivo *oxygen delivery and PDT assay*

For tumor oxygenation detection, the oxy- and deoxy-Hb levels in subcutaneous tumors were monitored through photoacoustic imaging using Vevo LAZR photoacoustic imager (Fujifilm Visual sonics, Amsterdam, the Netherlands) featuring a hybrid US transducer (central $f = 21$ MHz; spatial resolution = 75 µm). For experimental group, 200µl 5 nM lipid-GVs(O_2) were injected through tail vein, while mice with the injection of 200µl PBS(O_2) were used as control groups. Oxygen saturation of the tumors was measured before, during and after GVs treatment for 25 min. sO_2 levels were recorded and stored for later comparison between groups.

The effect of lipid-GVs(O_2) on PDT efficiency was evaluated on tumor-bearing mice models. ALA was administrated at the dose of 60 mg/kg through pure topical injection around the tumor 4 h before PDT treatment. The mice were randomly subdivided into five groups, including (1) control, (2) lipid-GVs(O_2) alone, (2) PDT, (3) PDT+ PBS(O_2), (4) PDT+ lipid-GVs(O_2). For the laser irradiation group, tumors were exposed to laser with a wavelength of 630 nm (deeper penetration than 405 nm) with the power of 100 mW/cm^2 for 20 min. The tumor size and bodyweight of each mouse were measured every 3 days following the treatment. The subcutaneous tumor volume was estimated by the following formula: Tumor volume ≈ largest diameter × smallest diameter^2/2. All mice were sacrificed on day 15 and tumor tissues were collected and fixed in 4% paraformaldehyde for 24 h, processed through conventional histological techniques and stained with hematoxylin and eosin (H&E). Images were captured by a Nikon optical microscope (Tokyo, Japan) and analysed using Nikon NIS-Elements software. For assessment of apoptosis in tumor sections, terminal deoxynucleotidyltransferase-mediated dUTP nick end labeling (TUNEL) was also carried out with an *in situ* Cell Death Detection Kit (Roche) following the manufacturer's protocol. Images were captured using a Nikon fluorescence microscope (Tokyo, Japan) and analyzed with Nikon NIS-Elements software.

2.8. In vitro *and* in vivo *toxicity determination*

For *in vitro* toxicity determination, two kinds of GVs (with final concentration 1 nM) were added into the cell culture media for different time point: 24 h, 48 h, and 72 h. After that, LDH assay was determined using the Pierce LDH Cytotoxicity Assay Kit (Thermo Fisher Scientific, MA, USA) according to the manufacturer's instructions. Cell viability and Cell Apoptosis was were also determined by MTT assay (Thermo Fisher Scientific, MA, USA) and Alexa Fluor 488 Annexin V/Dead Cell Apoptosis Kit (Thermo Fisher Scientific), respectively, according to the manufacturer's instructions. For *in vivo* toxicity determination, the body weight, food intake, and daily activity were observed before and after the experiments according to the handbook of health evaluation of experimental laboratory mice [30,47]. Post-mortem exams were also performed in mice and tissue samples (liver, lungs, and kidneys) were collected for histology. The liver, lung, and kidney samples collected from the mouse were also fixed in 4% Paraformaldehyde solution, processed with H&E staining as mentioned before.

2.9. *Statistical analyses*

Statistical analysis was performed with GraphPad Prism software. ImageJ, Photoshop CS and Illustrator CS software were used for image processing according to the general guidelines. Triplicate data were analyzed. Comparisons between two groups were made by Student's two-tailed *t*-test, and comparisons between more than two groups were made by one-way ANOVA followed by Bonferroni test. All data expressed as means ± SD. P-values <0.05 were considered statistically significant. Asterisks are used to indicate the significant differences.

3. Results and discussion

3.1. *Fabrication and characterization of lipid-GVs*

GVs for our study were produced by culturing the algae *Anabaena flos-aquae*, and isolating GVs through centrifugation. Since the shells of GVs are permeable to gas molecules, their oxygen delivery efficiency could be affected. Hence, we prepared GVs with surface modification using lipids (lipid-GVs) to reduce gas exchange [48,49] (Fig. 1). Native and lipid-GVs showed no major visible differences when in solution (Fig. 2A) or in the morphology of individual vesicles as observed by TEM (Fig. 2B). The lipid-GVs were next characterized for particle size distribution and zeta potential. These nanobubble formulations were found to have a mean diameter of approximately 300–330 nm and a uniform distribution (Fig. 2C,D). The average diameters of lipid-GVs were ~10 nm larger than native GVs, with a lower negative charge (Fig. 2E). The zeta potential of nanoparticles is closely associated with the stability of colloidal dispersions. Colloids with higher zeta potential (negative or positive, higher than 30) are electrically stabilized while colloids with lower zeta potential tend to coagulate easily [50]. The zeta potential of both GVs and lipid-GVs was found to be high enough to resist aggregation. We also evaluated the stability of the GVs in cold storage (4 °C). The concentration (determined by OD_{500}) and size of the two groups were observed from zero to six months and no significant changes were found in either group (Fig. 2F,G). We finally determined GV groups' stability in acidic PBS (pH 6) and FBS, respectively. GVs/lipid-GVs (final concentration =1 nM) were added to acidic PBS or FBS and incubated for 3 and 7 days, respectively. Over this period the concentration of all GV groups was found to decrease slightly but their concentrations always remained above 80% of the original (Fig. 2H). Thus, we were able to produce nanoscale, negatively charged GVs that were stable in solution through long-term storage.

3.2. *Determination of oxygen release kinetics of lipid-GVs*

We next tested the oxygen release kinetics of the groups by their abilities to raise oxygen concentrations in hypoxic solutions. We found that lipid-GVs(O_2) could increase the oxygen concentration of severely hypoxic solutions significantly compared to oxygen-filled PBS (Fig. 3). Compared to native GVs(O_2), lipid-GVs(O_2) showed a significantly greater ability to elevate the solution's oxygen concentration. The release of oxygen by lipid-GVs(O_2) into solution was also slower than native GVs(O_2). We attribute this to the surface modification of GVs leading to slower oxygen release kinetics. Moreover, the ability of GVs to release oxygen was found to be concentration-dependent, with a higher concentration displaying greater ability to raise oxygen concentration of hypoxic solutions. Thus, compared to native GVs, lipid-GVs showed slower release patterns and were able to increase the oxygen concentration to a greater degree.

3.3. In vitro *oxygen delivery detection and PDT assay*

We next evaluated lipid-GVs' abilities to modify the hypoxic conditions of cells *in vitro*. Human hepatoma cells (HepG2 cell line) were grown in hypoxic conditions overnight and levels of hypoxia were monitored using Image-iT Red Hypoxia Reagent. Compared to the untreated control and PBS(O_2), the addition of lipid-GVs(O_2) significantly reduced the observed levels of hypoxia (Fig. 4A,B). We next tested whether lipid-GVs(O_2) could increase

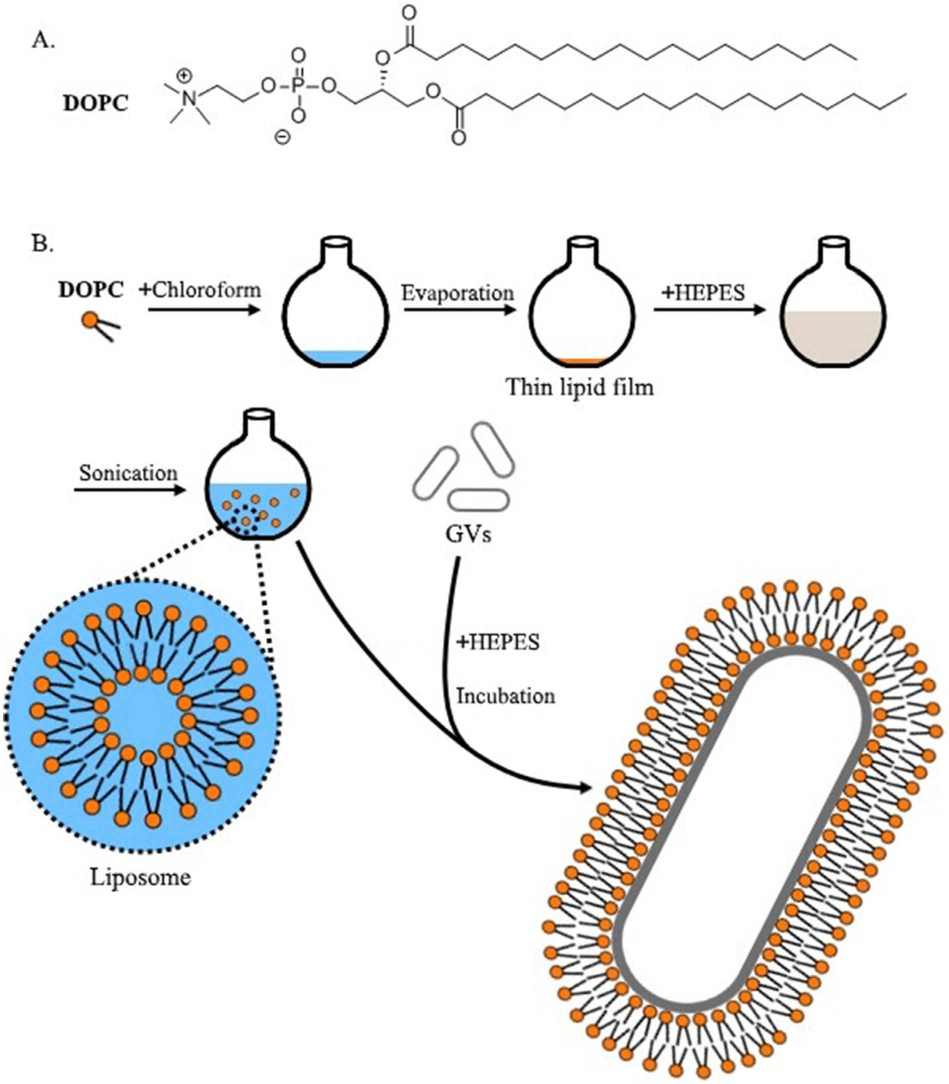

Fig. 1. Illustration of the chemical process to fabricate lipid-GVs. (A) Molecular structure of DOPC. (B) Schematic overview of the preparation of lipid-GVs.

the efficacy of PDT under hypoxic conditions. A schematic illustration of our PDT setup is shown in Fig. 4C. The impact of adding lipid-GVs(O_2) on the cytotoxicity of ALA-PDT, in hypoxic HepG2 cells was determined using a CCK-8 assay, 4 h after PDT treatment. PDT alone decreased cell viability of HepG2 cells to 85%, while the addition of lipid-GVs(O_2) significantly decreased cell viability following PDT to 50% (Fig. 4D). We also investigated the effects of lipid-GVs(O_2) on PDT induced cell apoptosis by flow cytometry for PI/Annexin V. Consistent with the aforementioned results, the addition of lipid-GVs(O_2) increased the rate of necrosis and apoptosis among cells by nearly 20% following PDT compared to the PBS(O_2) group (Fig. 4E). Crucially, lipid-GVs(O_2) alone had no effect on cell viability and apoptosis. These data demonstrate that the addition of lipid-GVs(O_2) could lead to significantly higher cell death and apoptosis levels of cancer cells following PDT. Excessive production of ROS is believed to be the mechanism responsible for the cytotoxicity of tumor cells during PDT. Hence, we further investigated whether the addition of lipid-GVs(O_2) increased the production of intracellular ROS following PDT. As expected, excessive ROS production was detected 1 h following PDT in all three PDT treatment groups, but total intracellular ROS was most significantly increased with the addition of lipid-GVs(O_2) (Fig. 4F,G).

3.4. In vivo *biodistribution and tumor accumulation of lipid-GVs*

To monitor the biodistribution of the lipid-GVs *in vivo*, we labeled lipid-GVs with indocyanine green (ICG), a near infra-red (NIR) fluorophore. ICG-labeled lipid-GVs showed an absorption peak around 800 nm, indicating the successful incorporation of ICG into lipid-GVs (Fig. 5A). Fluorescent imaging of both ICG and ICG-labeled lipid-GVs showed strong fluorescence, indicating the incorporation of ICG into lipid-GVs had minimal effects on ICG's fluorescent properties (Fig. 5B). For *in vivo* real-time NIRF imaging, tumor-bearing nude mice were monitored for 2 h after systemic administration of 200 µl PBS, free ICG (20 µg) and 5 nM ICG-labeled lipid-GVs (containing 20 µg ICG), respectively. Both free ICG and ICG-labeled lipid-GVs showed significant fluorescence in the vital organs (liver, lungs, spleen, etc.) within one hour and decreased over time (Fig. 5C). The ICG signal in the tumor peaked at half an hour after injection, indicating rapid tumor clearance, whereas the tumor fluorescence in the ICG-labeled lipid-GVs group was detectable from 5 min to 2 h after injection (Fig. 5D and F). Closer examination of the fluorescence signals from major organs of both groups showed high fluorescence intensity occurred mainly in the liver and kidney within two hours and decreased over time

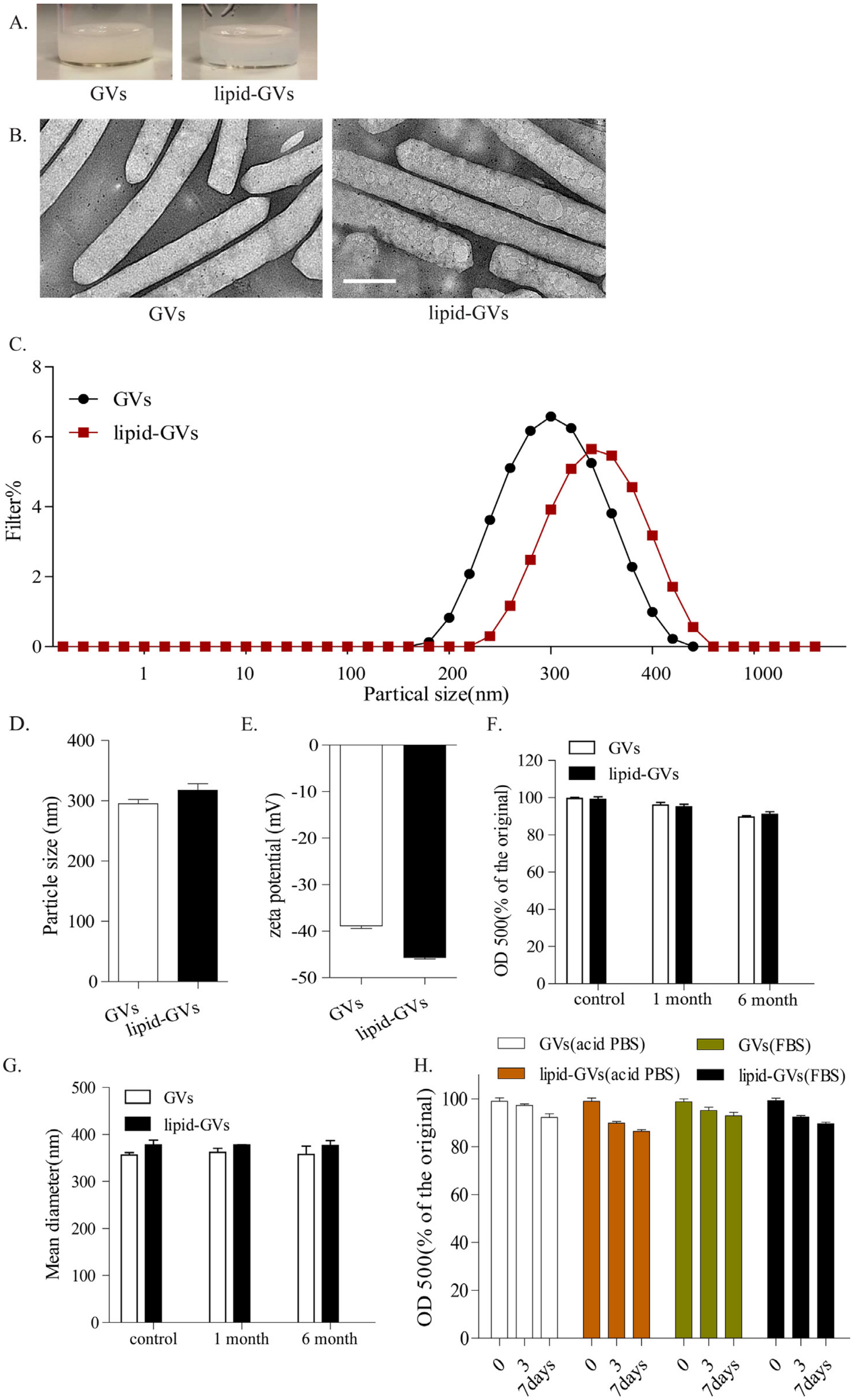

Fig. 2. Morphology, size distribution, and zeta potential of native GVs and lipid-GVs. (A) Photographic images of 1 nM GVs and lipid-GVs in solution. (B) The TEM image of GVs, showing their morphology (images are representative). Scale bar represents 100 nm. (C) Histogram showing the relative size distributions of the two GV groups with the statistics shown in (D). (E) Zeta potential statistics of two GV groups. (F) GV groups' stability over 6 months observed by measuring their concentration. (G) GV groups' stability over 6 months observed by measuring their size. Data in (D) - (G) represent the mean ± SD from 3 independent experiments. (H) GV groups' stability in acidic PBS (pH 6) and neutral FBS was determined by measuring their concentration. Data represent the mean ± SD from 3 independent experiments.

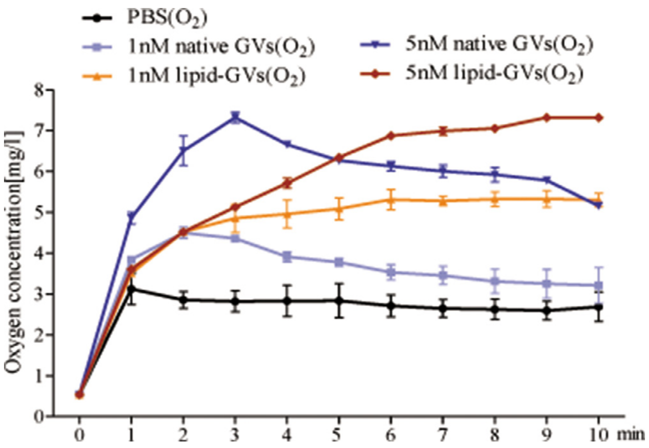

Fig. 3. Determination of oxygen release kinetics of GVs. The oxygen concentration in 5 ml severe hypoxic solution after injection of 1 ml of PBS(O_2), GVs(O_2) or lipid-GVs(O_2). Data represent the mean ± SD based on 3 independent experiments.

(Fig. 5E, G and H).Thus, lipid-GVs were able to be retained in tumors for at least 2 h post-injection, which would be a long enough period for oxygen delivery.

3.5. In vivo *oxygen delivery detection and PDT assay of lipid-GVs*

Lipid-GVs' abilities to modify the hypoxic conditions of tumor masses *in vivo* were evaluated. An *in vivo* proof-of-concept experiment was also performed to determine the ability of lipid-GVs(O_2) to elevate hypoxic subcutaneous tumor oxygenation levels in nude mice. Tumor oxygenation was monitored by visualizing the levels of oxy-Hemoglobin (oxy-Hb) and deoxy-Hemoglobin (deoxy-Hb) through photoacoustic imaging before and after the treatment (0, 5, 15, and 25 min). Tail-vein injection of lipid-GVs(O_2) resulted in elevated sO_2 in the tumors and sO_2 peaked 15 min following injection and then decreased gradually, but not with the PBS(O_2) controls (Fig. 6A,B). Thus, we found that the lipid-GVs filled with O_2 were successfully able to raise oxygen levels in subcutaneous tumors.

The effects of lipid-GVs(O_2) on ALA-mediated PDT *in vivo* was then evaluated. Treatments were begun when subcutaneous tumor volume reached 300 mm^3. 200 µl lipid-GVs(O_2) were intravenous injected into mice 15 min before laser irradiation. Tumor volumes and body weight were measured every three days after various treatments. Rapid and continuous growth of tumor was observed in both control group and lipid-GVs(O_2) alone group for the following 15 days with the volume of tumors reaching nearly 1500mm^3 at the end of the experiments on the 15th day (Fig. 6C). For PDT treatment groups, all three groups exhibited effective tumor growth inhibition efficacy compared to control group and lipid-GVs(O_2) alone group. Tumors were found to shrink significantly in the early three days following PDT treatment and to regrow slowly by the end of test period. However, even compared to all the groups with PDT, lipid-GVs(O_2) showed significantly greater tumor growth inhibition, being the lowest of all five tested groups. Crucially, PDT plus PBS(O_2) treatment showed negligible effects compared to PDT alone, again indicating the important ability of lipid-GVs to successfully carry *and* to deliver O_2 to the tumor site. The body weights of mice were also recorded during the experiments to assess the systematic toxicity of the treatment, and no significant change was detected among the five groups (Fig. 6D). However, a gradual increase in body weight was seen in the control group and lipid-GVs(O_2) alone group, which may have been caused by rapid tumor growth. To further confirm the role of lipid-GVs(O_2) in improving the therapeutic efficacy of PDT, H&E staining and TUNEL assay of tumor slices were obtained. Compared to control group and lipid-GVs(O_2) alone group, which showed normal morphology, H&E staining in PDT, PDT +PBS(O_2) and PDT+lipid-GVs(O_2) groups revealed severe damage, with PDT+lipid-GVs(O_2) group showing the most significant toxicity effects (Fig. 6E). Similarly, a TUNEL assay revealed much higher levels of apoptosis in PDT+lipid-GVs(O_2) than in the PDT and PDT+PBS(O_2) groups, with almost no apoptosis in control and lipid-GVs(O_2) alone groups (Fig. 6F). Taken together, these results demonstrate the efficacy of lipid-GVs(O_2) to enhance PDT outcomes. These data also highlight that while PDT+PBS(O_2) showed some effects *in vitro*, it much less effective than PDT+lipid-GVs(O_2) *in vivo*, emphasizing lipid-GVs' capability to successfully deliver O_2 to the tumor site after systemic injection.

3.6. In vitro *and* in vivo *toxicity detection*

Finally, we tested the toxicity and biosafety of both GVs and lipid-GVs. We used the LDH, MTT and apoptosis assays *in vitro* for this purpose and found that both GVs and lipid-GVs triggered no cytotoxicity on cells. GVs/lipid-GVs (final concentration=1 nM) were added to the culture medium and incubate for 24, 48 or 72 h. No significant elevation in LDH, formazan levels, Annexin V or PI signal was observed at any time point, compared to the control (Fig. 7A–C). We next tested the biosafety of GVs/lipid-GVs *in vivo* by observing three basic measures of mouse health (activity, weight and food intake) before the administration of GVs/lipid-GVs, and 24, 48 and 72 h after administration of GVs/Lipid-GVs. Scoring the mice on a 30-point scale, we observed no decrease in these indicators over the time period (Fig. 7D). We also assayed the mice's major organs (heart, liver, spleen, lungs, and kidneys) one week after GVs/lipid-GVs' administration using hematoxylin and eosin (H&E) staining (Fig. 7E). Tissue slices from both GVs' and lipid-GVs' groups presented no significant pathological abnormalities or lesions compared to the control group. We thus determined that both GVs and lipid-GVs alone were not cytotoxic to cells and did not cause any significant damage to the mice in which they were tested.

4. Conclusion

In the present study, we present gas vesicles as promising oxygen nanocarriers to alleviate tumor hypoxia. As a type of physically stable nanostructure, GVs kept very well in long-term storage in cool conditions as well as in acidic conditions over a week. Preliminary *in vitro* results showed lipid-GVs(O_2) could change the hypoxic condition of cell culture when added to the medium. This indicates that lipid-GVs can carry enough oxygen to significantly affect cell culture. Our preliminary *in vivo* biodistribution results in tumor-bearing mice showed that lipid-GVs could be detected in the tumor site up to two hours post-injection, indicating that lipid-GVs were stable enough to survive the circulation to the tumor site. Besides, *in vivo* oxygen delivery results also showed the ability of lipid-GVs(O_2) to elevate oxygenation levels in hypoxic tumors *in vivo* 5 min after tail injection, indicating their ability to deliver a significant amount of oxygen. The PDT assays *in vitro* and *in vivo* showed that the addition of lipid-GVs(O_2) could enhance the photodynamic effect. Toxicity studies both *in vitro* and *in vivo* showed lipid-GVs to be well tolerated. Compared to other organic or inorganic materials which could lead to adverse effects, the initial biocompatibility of GVs was seen to be good and safe for mice. The observed long-term storage in cold conditions, good oxygen-loading and release capabilities, and no acute toxicity makes lipid-GVs unique among other oxygen carriers. Thus, our approach provided a new choice for oxygen delivery to tumor site for PDT as well as other oxygen-consuming tumor therapies.

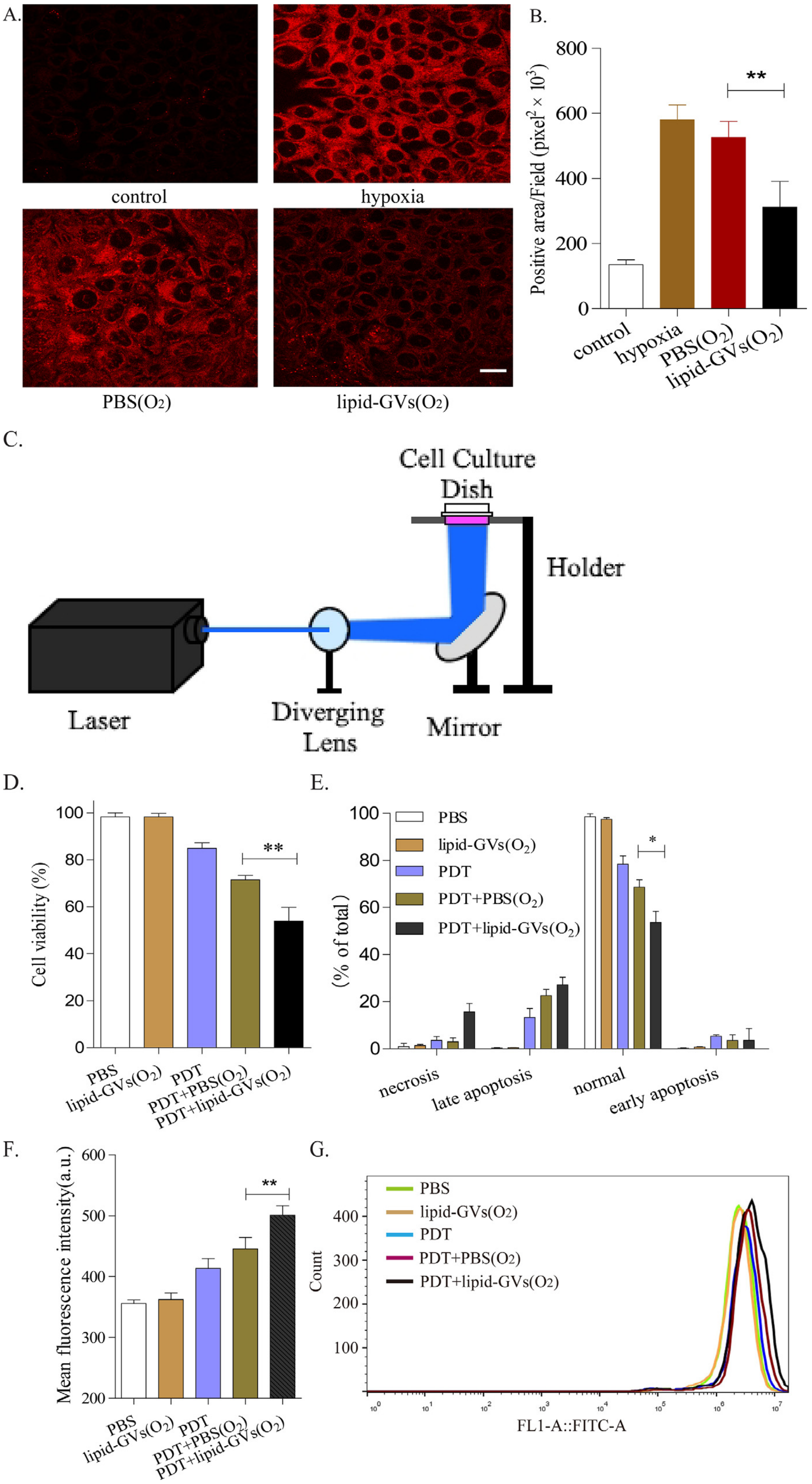

Fig. 4. Lipid-GVs(O_2) mediated oxygen delivery and PDT under hypoxia *in vitro*. (A) 200 µl PBS(O_2) or lipid-GVs(O_2) (with final concentration 1 nM) was added into medium and cultured with cells in hypoxic condition for 1 h. Image-iT Red Hypoxia Reagent was used to detect hypoxia in cultured cells, indicated by red fluorescence. Representative images are shown in (A) with quantification of hypoxic staining shown in (B). Data represent the mean ± SD from on 3 independent experiments. $^{**}p < 0.01$ vs. control. Scale bar represents 25 µm. (C) Schematic diagram of PDT setup. (D) Relative cell viability of HepG2 cells after different treatments by CCK-8 assay. Data represent mean ± SD of 3 independent experiments. $^{**}p < 0.01$ vs. PBS. (E) Evaluation of cell apoptosis following different treatments by flow cytometry through Annexin-V and propidium iodide (PI) double staining. Data represent the mean ± SD based on 3 independent experiments. $^{*}p < 0.05$ vs. PBS. (F) Intracellular ROS generation stained with DCFHDA and analyzed by flow cytometry following different treatments. The values are the mean ± SD of three independent experiments. $^{**}p < 0.01$ vs. pbs. Overlapping image of five groups is shown in (G). (For interpretation of the references to color in this figure legend, the reader is referred to the web version of this article.)

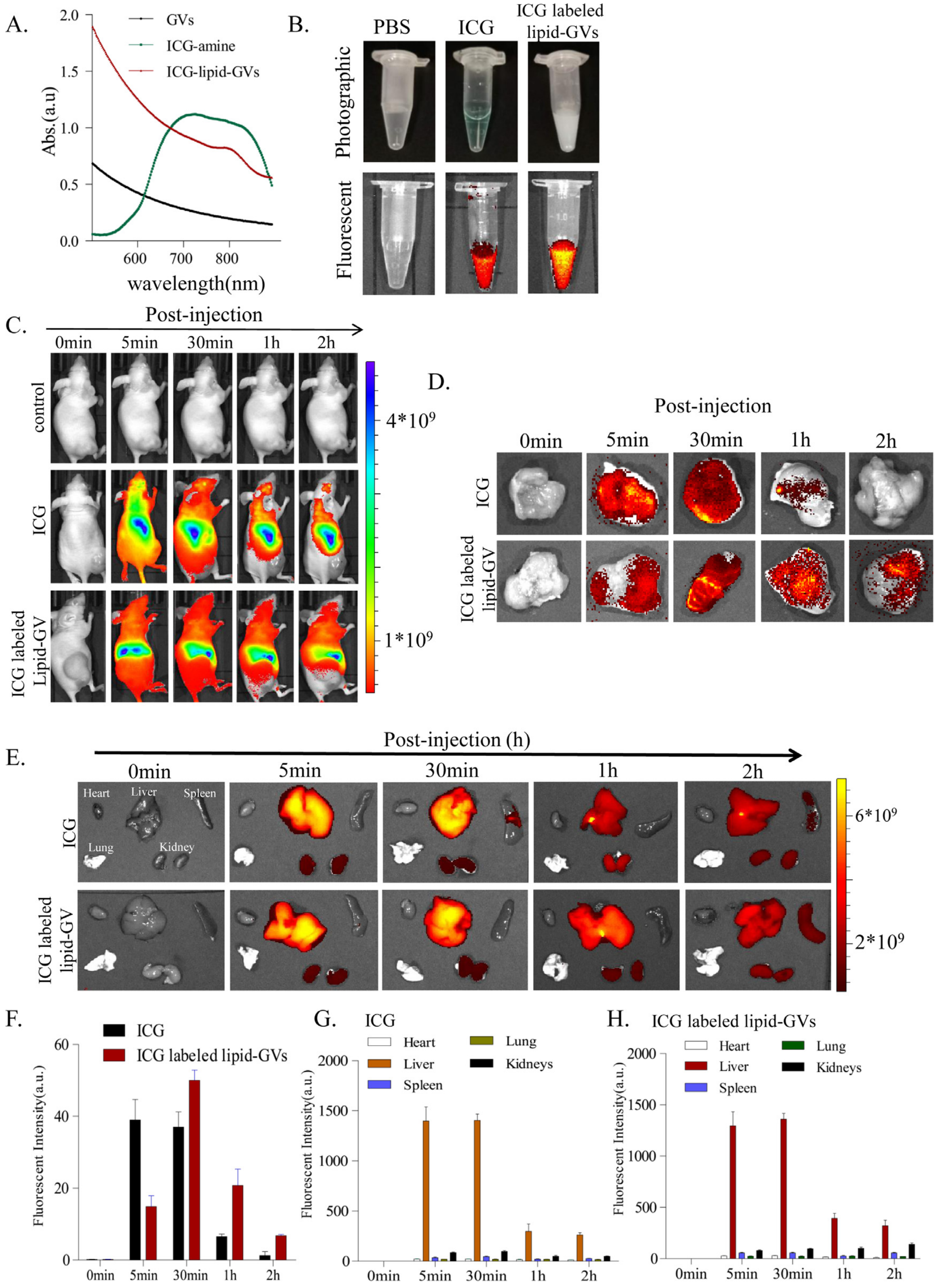

Fig. 5. *In vivo biodistribution of ICG labeled lipid-GVs.* (A) Absorbance spectra of native GVs, ICG, ICG labeled lipid-GVs in phosphate buffered saline (PBS). (B) Photographic and fluorescent images of ICG and ICG labeled lipid-GVs (Ex. 780 nm, Em. 845 nm). (C) *In vivo* NIR fluorescent imaging of tumor-bearing nude mice at different time after intravenous injection of free ICG and ICG labeled lipid-GVs, respectively. Ex vivo fluorescence imaging of tumors and vital organs from tumor-bearing nude mice after different timepoints post-injection of ICG and ICG-labeled lipid-GVs, respectively. Representative images were shown in (D) and (E), respectively. Quantitative analysis is shown in (F), (G) and (H), respectively. Data represent the mean ± SD ($n = 4$).

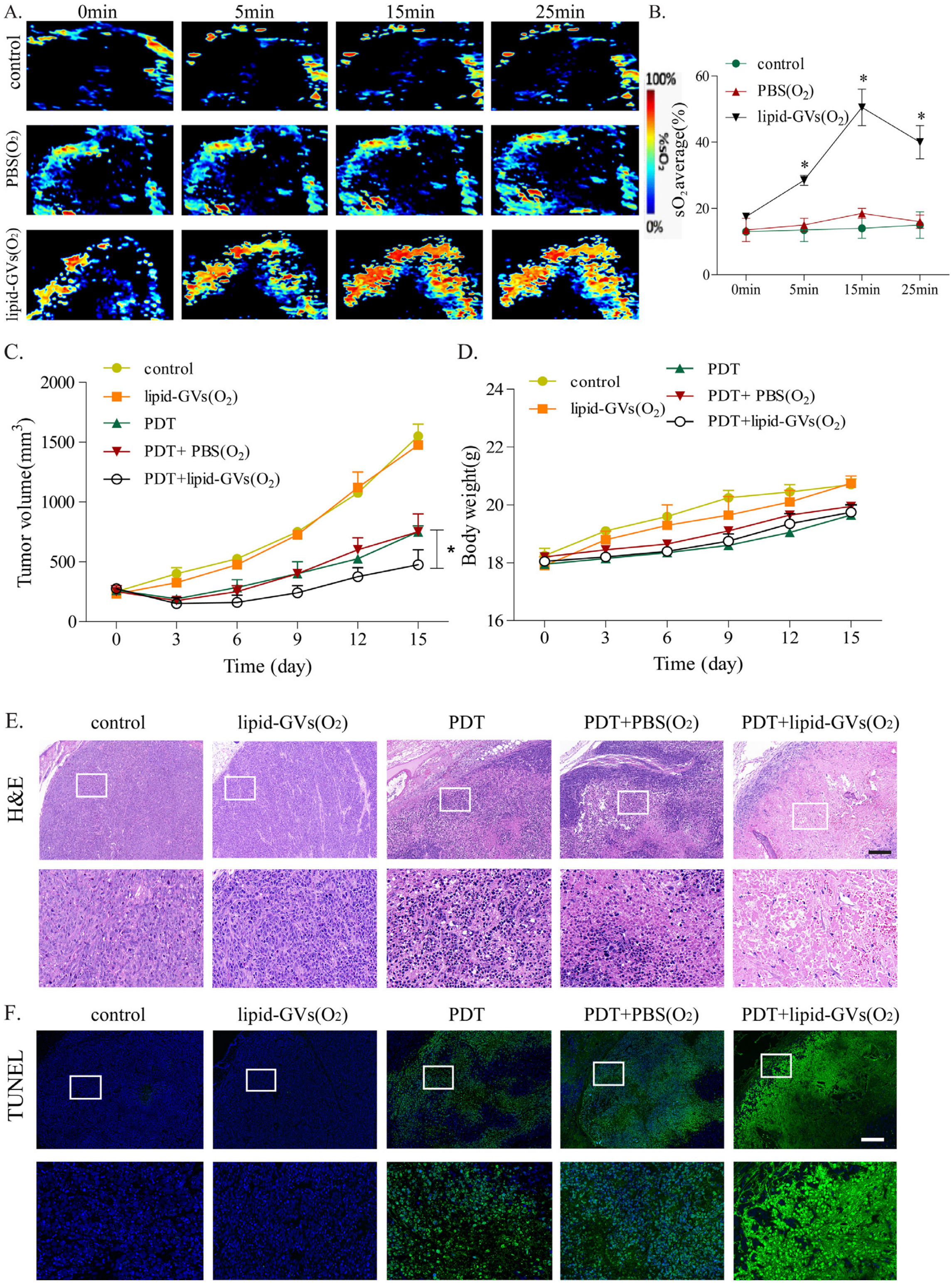

Fig. 6. Lipid-GVs(O_2) mediated oxygen delivery and PDT *in vivo*. (A) Representative photoacoustic images of tumor oxygen levels (Oxy-Hb and deoxy-Hb levels) from *in vivo* tumor-bearing mice at different time points by tail vein injection of 200 µl of saline, PBS(O_2), and 5 nM lipid-GVs(O_2). Red pixels: oxy-Hb; blue pixels: deoxy-Hb. (B) Quantification of tumor oxygen levels. Data represent the mean ± SD based on 4 independent experiments. $^*p < 0.05$ vs. control. (C) Effects of lipid-GVs(O_2) on *in vivo* PDT were determined. Tumor growth curves of SCC7 tumor-bearing mice with different treatment groups. $n = 5$ mice per group, $^*p < 0.05$ significance level. (D) Body weight of SCC7 tumor-bearing mice after various treatments. (E) Representative histological images of H&E stained tumor slices collected from different groups. Scale bar represents 200 µm. (F) Representative images of TUNEL assay of tumor slices collected from different groups. Scale bar represents 200 µm. (For interpretation of the references to color in this figure legend, the reader is referred to the web version of this article.)

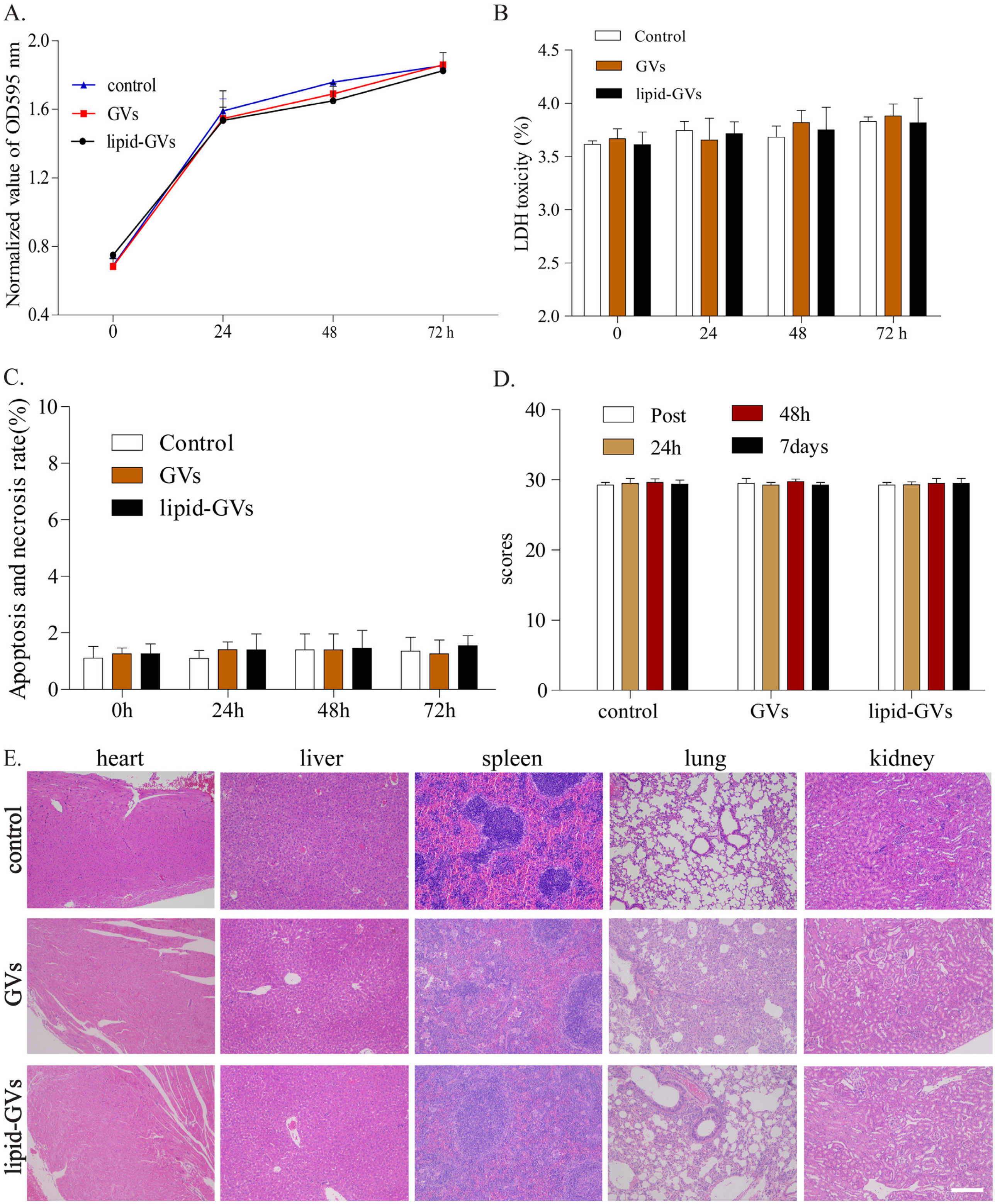

Fig. 7. Toxicity of GVs/ lipid-GVs both *in vitro* and *in vivo*. (A,B) 200 µl GVs/ lipid-GVs (final concentration 1 nM) were added into media the media incubated with HepG2 cells for multiple days. Cell proliferation and LDH toxicity of HepG2 cells were measured by MTT and LDH assay at the time points indicated. Data represent the mean ± SD based on 3 independent experiments. (C) Apoptosis in HepG2 cells were measured by Annexin V and PI assay at the various time points indicated. Data represent the mean ± SD based on 3 independent experiments. (D) The overall scores of mice indicating their observed health condition. Mice were scored on a 30-point scale comprising 10 points each for activity, weight, food intake. The assessment was performed before, immediately after, 24 h, 48 h and one week after injection ($N = 5$, ±SD). (E) Histological images of major organs with H&E staining collected from mice treated with GVs/ lipid-GVs on day 7. Scale bar represents 100 µm.

Besides being mere oxygen carriers, the shells of GVs are readily linkable with various anti-tumor drugs, GVs have the potential to be an effective carrier for both oxygen and drug delivery into tumor sites with potentially long circulation time and high efficacy. Furthermore, GVs can be used as a contrast agent for ultrasonic imaging due to the echogenicity of gas core [34,51–53]. Further work is still needed to confirm whether they have prolonged intravascular retention time, whether they could induce allergic or immunologic reactions during transfusions or whether they could induce potential long term immunotoxicity. Crucially, even any of these issues emerge in further testing, the possibility of alleviating or eliminating these effects through surface modification would still remain, giving such GVs an even greater chance of being successful. Thus, GVs are a versatile entity that could be used to combine multiple aspects of cancer therapy, potentially achieving the aim of ultrasound-guided oxygen delivery and therapy. Such approaches could help to pave the way for the era of better-targeted cancer therapies with reduced side-effects and greater efficacies.

Declaration of Competing Interest

The authors declare that they have no known competing financial interests or personal relationships that could have appeared to influence the work reported in this paper.

Acknowledgments

The authors would like to thank the facility and technical support from University Research Facility in Life Sciences (ULS) of The Hong Kong Polytechnic University in this work. This work was financially supported through grants from the General Research Fund (project #15215615 and 15326416), Health and Medical Research Fund (03144266) and Natural Science Foundation of China (project # 11674271).

References

[1] S.V. Karakashev, M.J. Reginato, Progress toward overcoming hypoxia-induced resistance to solid tumor therapy, Cancer Manag. Res. 7 (2015) 253–264.
[2] B. Muz, P. de la Puente, F. Azab, A.K. Azab, The role of hypoxia in cancer progression, angiogenesis, metastasis, and resistance to therapy, Hypoxia Auckl. 3 (2015) 83–92.
[3] M.C. Bosco, G. D'Orazi, D. Del Bufalo, Targeting hypoxia in tumor: a new promising therapeutic strategy, J. Exp. Clin. Cancer Res. 39 (1) (2020) 8.
[4] X. Zhou, H. Liu, Y. Zheng, Y. Han, T. Wang, H. Zhang, Q. Sun, Z. Li, Overcoming radioresistance in tumor therapy by alleviating hypoxia and using HIF-1 inhibitor, ACS Appl. Mater. Interfaces 12 (4) (2020) 4231–4240.
[5] I. Moen, L.E. Stuhr, Hyperbaric oxygen therapy and cancer–a review, Target Oncol. 7 (4) (2012) 233–242.
[6] K. Stepien, R.P. Ostrowski, E. Matyja, Hyperbaric oxygen as an adjunctive therapy in treatment of malignancies, including brain tumours, Med. Oncol. 33 (9) (2016) 101.
[7] M. Heyboer 3rd., D. Sharma, W. Santiago, N. McCulloch, Hyperbaric oxygen therapy: side effects defined and quantified, Adv. Wound Care 6 (6) (2017) 210–224.
[8] S. Moradi, A. Jahanian-Najafabadi, M.H. Roudkenar, Artificial blood substitutes: first steps on the long route to clinical utility, Clin. Med. Insights Blood Disord. 9 (2016) 33–41.
[9] F. Alam, N. Yadav, M. Ahmad, M. Shadan, Blood substitutes: possibilities with nanotechnology, Indian J. Hematol. Blood Transfus. 30 (3) (2014) 155–162.
[10] C.L. Varnado, T.L. Mollan, I. Birukou, B.J. Smith, D.P. Henderson, J.S. Olson, Development of recombinant hemoglobin-based oxygen carriers, Antioxid. Redox Signal 18 (17) (2013) 2314–2328.
[11] J.R. Eisenbrey, L. Albala, M.R. Kramer, N. Daroshefski, D. Brown, J.B. Liu, M. Stanczak, P. O'Kane, F. Forsberg, M.A. Wheatley, Development of an ultrasound sensitive oxygen carrier for oxygen delivery to hypoxic tissue, Int. J. Pharm. 478 (1) (2015) 361–367.
[12] S.M. Fix, M.A. Borden, P.A. Dayton, Therapeutic gas delivery via microbubbles and liposomes, J. Control Release 209 (2015) 139–149.
[13] J.J. Kwan, M. Kaya, M.A. Borden, P.A. Dayton, Theranostic oxygen delivery using ultrasound and microbubbles, Theranostics 2 (12) (2012) 1174–1184.
[14] E.J. Swanson, V. Mohan, J. Kheir, M.A. Borden, Phospholipid-stabilized microbubble foam for injectable oxygen delivery, Langmuir 26 (20) (2010) 15726–15729.
[15] M.S. Khan, J. Hwang, K. Lee, Y. Choi, K. Kim, H.J. Koo, J.W. Hong, J. Choi, Oxygen-carrying micro/nanobubbles: composition, synthesis techniques and potential prospects in photo-triggered theranostics, Molecules 23 (9) (2018) 2210.
[16] T. Luo, J. Sun, S. Zhu, J. He, L. Hao, L. Xiao, Y. Zhu, Q. Wang, X. Pan, Z. Wang, S. Chang, Ultrasound-mediated destruction of oxygen and paclitaxel loaded dual-targeting microbubbles for intraperitoneal treatment of ovarian cancer xenografts, Cancer Lett. 391 (2017) 1–11.
[17] J.R. Eisenbrey, R. Shraim, J.B. Liu, J. Li, M. Stanczak, B. Oeffinger, D.B. Leeper, S.W. Keith, L.J. Jablonowski, F. Forsberg, P. O'Kane, M.A. Wheatley, Sensitization of hypoxic tumors to radiation therapy using ultrasound-sensitive oxygen microbubbles, Int. J. Radiat. Oncol. Biol. Phys. 101 (1) (2018) 88–96.
[18] B.D. Polizzotti, L.M. Thomson, D.W. O'Connell, F.X. McGowan, J.N. Kheir, Optimization and characterization of stable lipid-based, oxygen-filled microbubbles by mixture design, J. Biomed. Mater. Res. B Appl. Biomater. 102 (6) (2014) 1148–1156.
[19] J.N. Kheir, B.D. Polizzotti, L.M. Thomson, D.W. O'Connell, K.J. Black, R.W. Lee, J.N. Wilking, A.C. Graham, D.C. Bell, F.X. McGowan, Bulk manufacture of concentrated oxygen gas-filled microparticles for intravenous oxygen delivery, Adv. Healthc. Mater. 2 (8) (2013) 1131–1141.
[20] K.H. Martin, P.A. Dayton, Current status and prospects for microbubbles in ultrasound theranostics, Wiley Interdiscip. Rev. Nanomed. Nanobiotechnol. 5 (4) (2013) 329–345.
[21] C. Liu, F. Yan, Y. Xu, H. Zheng, L. Sun, InVivo molecular ultrasound assessment of glioblastoma neovasculature with endoglin-targeted microbubbles, Contrast Media Mol. Imaging 2018 (2018) 8425495.
[22] S. Zullino, M. Argenziano, I. Stura, C. Guiot, R. Cavalli, From micro- to nano-multifunctional theranostic platform: effective ultrasound imaging is not just a matter of scale, Mol. Imaging 17 (2018) 1536012118778216.
[23] Y. Nakamura, A. Mochida, P.L. Choyke, H. Kobayashi, Nanodrug delivery: is the enhanced permeability and retention effect sufficient for curing cancer? Bioconjug. Chem. 27 (10) (2016) 2225–2238.
[24] R. Ngoune, A. Peters, D. von Elverfeldt, K. Winkler, G. Putz, Accumulating nanoparticles by EPR: a route of no return, J. Control Release 238 (2016) 58–70.
[25] R. Cavalli, A. Bisazza, P. Giustetto, A. Civra, D. Lembo, G. Trotta, C. Guiot, M. Trotta, Preparation and characterization of dextran nanobubbles for oxygen delivery, Int. J. Pharm. 381 (2) (2009) 160–165.
[26] R. Song, D. Hu, H.Y. Chung, Z. Sheng, S. Yao, Lipid-polymer bilaminar oxygen nanobubbles for enhanced photodynamic therapy of cancer, ACS Appl. Mater. Interfaces 10 (43) (2018) 36805–36813.
[27] M.S. Khan, J. Hwang, Y. Seo, K. Shin, K. Lee, C. Park, Y. Choi, J.W. Hong, J. Choi, Engineering oxygen nanobubbles for the effective reversal of hypoxia, Artif. Cells Nanomed. Biotechnol. 46 (sup3) (2018) S318–S327.
[28] M.S. Khan, J. Hwang, K. Lee, Y. Choi, J. Jang, Y. Kwon, J.W. Hong, J. Choi, Surface composition and preparation method for oxygen nanobubbles for drug delivery and ultrasound imaging applications, Nanomaterials 9 (1) (2019).
[29] H.S. Min, D.G. You, S. Son, S. Jeon, J.H. Park, S. Lee, I.C. Kwon, K. Kim, Echogenic glycol chitosan nanoparticles for ultrasound-triggered cancer theranostics, Theranostics 5 (12) (2015) 1402–1418.
[30] M.G. Shapiro, P.W. Goodwill, A. Neogy, M. Yin, F.S. Foster, D.V. Schaffer, S.M. Conolly, Biogenic gas nanostructures as ultrasonic molecular reporters, Nat. Nanotechnol. 9 (4) (2014) 311–316.
[31] D.I. Piraner, A. Farhadi, H.C. Davis, D. Wu, D. Maresca, J.O. Szablowski, M.G. Shapiro, Going deeper: biomolecular tools for acoustic and magnetic imaging and control of cellular function, Biochemistry 56 (39) (2017) 5202–5209.
[32] D. Maresca, A. Lakshmanan, M. Abedi, A. Bar-Zion, A. Farhadi, G.J. Lu, J.O. Szablowski, D. Wu, S. Yoo, M.G. Shapiro, Biomolecular ultrasound and sonogenetics, Annu. Rev. Chem. Biomol. Eng. 9 (2018) 229–252.
[33] G. Wang, L. Song, X. Hou, S. Kala, K.F. Wong, L. Tang, Y. Dai, L. Sun, Surface–modified GVs as nanosized contrast agents for molecular ultrasound imaging of tumor, Biomaterials 236 (2020) 119803.
[34] Y. Yang, Z. Qiu, X. Hou, L. Sun, Ultrasonic characteristics and cellular properties of anabaena gas vesicles, Ultrasound Med. Biol. 43 (12) (2017) 2862–2870.
[35] F. Pfeifer, Haloarchaea and the formation of gas vesicles, Life 5 (1) (2015) 385–402.
[36] A. Lakshmanan, A. Farhadi, S.P. Nety, A. Lee-Gosselin, R.W. Bourdeau, D. Maresca, M.G. Shapiro, Molecular engineering of acoustic protein nanostructures, ACS Nano 10 (8) (2016) 7314–7322.
[37] P. Agostinis, K. Berg, K.A. Cengel, T.H. Foster, A.W. Girotti, S.O. Gollnick, S.M. Hahn, M.R. Hamblin, A. Juzeniene, D. Kessel, M. Korbelik, J. Moan, P. Mroz, D. Nowis, J. Piette, B.C. Wilson, J. Golab, Photodynamic therapy of cancer: an update, CA Cancer J. Clin. 61 (4) (2011) 250–281.
[38] D. van Straten, V. Mashayekhi, H.S. de Bruijn, S. Oliveira, D.J. Robinson, Oncologic photodynamic therapy: basic principles, current clinical status and future directions, Cancers 9 (2) (2017).
[39] C. Zhang, X. Cheng, M. Chen, J. Sheng, J. Ren, Z. Jiang, J. Cai, Y. Hu, Fluorescence guided photothermal/photodynamic ablation of tumours using pH-responsive chlorin e6-conjugated gold nanorods, Colloids Surf. B Biointerfaces 160 (2017) 345–354.
[40] C. Zhang, J. Ren, J. Hua, L. Xia, J. He, D. Huo, Y. Hu, Multifunctional Bi2WO6 nanoparticles for CT-Guided photothermal and oxygen-free photodynamic therapy, ACS Appl. Mater. Interfaces 10 (1) (2018) 1132–1146.
[41] P. Zhao, S. Ren, Y. Liu, W. Huang, C. Zhang, J. He, PL-W18O49-TPZ nanoparticles for simultaneous hypoxia-activated chemotherapy and photothermal therapy, ACS Appl. Mater. Interfaces 10 (4) (2018) 3405–3413.
[42] H. Zuo, J. Tao, H. Shi, J. He, Z. Zhou, C. Zhang, Platelet-mimicking nanoparti-

cles co-loaded with W18O49 and metformin alleviate tumor hypoxia for enhanced photodynamic therapy and photothermal therapy, Acta Biomater. 80 (2018) 296–307.

[43] F. Xu, A. Bandara, H. Akiyama, B. Eshaghi, D. Stelter, T. Keyes, J.E. Straub, S. Gummuluru, B.M. Reinhard, Membrane-wrapped nanoparticles probe divergent roles of GM3 and phosphatidylserine in lipid-mediated viral entry pathways, Proc. Natl. Acad. Sci. U. S. A. 115 (39) (2018) E9041–E9050.

[44] F. Tamura, Y. Tanimoto, R. Nagai, F. Hayashi, K. Morigaki, Self-spreading of phospholipid bilayer in a patterned framework of polymeric bilayer, Langmuir 35 (45) (2019) 14696–14703.

[45] D. Stelter, T. Keyes, Lipid packing in lipid-wrapped nanoparticles, J. Phys. Chem. B 122 (26) (2018) 6755–6762.

[46] J.C. Kraft, R.J. Ho, Interactions of indocyanine green and lipid in enhancing near-infrared fluorescence properties: the basis for near-infrared imaging *in vivo*, Biochemistry 53 (8) (2014) 1275–1283.

[47] T. Burkholder, C. Foltz, E. Karlsson, C.G. Linton, J.M. Smith, Health evaluation of experimental laboratory mice, Curr. Protoc. Mouse Biol. 2 (2012) 145–165.

[48] M.A. Borden, M.L. Longo, Oxygen permeability of fully condensed lipid monolayers, J. Phys. Chem. B 108 (19) (2004) 6009–6016.

[49] J.J. Kwan, M.A. Borden, Lipid monolayer dilatational mechanics during microbubble gas exchange, Soft Matter 8 (17) (2012).

[50] S. Honary, F. Zahir, Effect of zeta potential on the properties of nano-drug delivery systems - a review (Part 2), Trop. J. Pharm. Res. 12 (2) (2013).

[51] G.J. Lu, A. Farhadi, J.O. Szablowski, A. Lee-Gosselin, S.R. Barnes, A. Lakshmanan, R.W. Bourdeau, M.G. Shapiro, Acoustically modulated magnetic resonance imaging of gas-filled protein nanostructures, Nat. Mater. 17 (5) (2018) 456–463.

[52] J.P. Feser, J. Ravichandran, More power to pyroelectrics, Nat. Mater. 17 (5) (2018) 385–386.

[53] A. Lakshmanan, G.J. Lu, A. Farhadi, S.P. Nety, M. Kunth, A. Lee-Gosselin, D. Maresca, R.W. Bourdeau, M. Yin, J. Yan, C. Witte, D. Malounda, F.S. Foster, L. Schroder, M.G. Shapiro, Preparation of biogenic gas vesicle nanostructures for use as contrast agents for ultrasound and MRI, Nat. Protoc. 12 (10) (2017) 2050–2080.